Journal of Theoretical Biology 390 (2016) 136–145

Contents lists available at ScienceDirect

Journal of Theoretical Biology

journal homepage: www.elsevier.com/locate/yjtbi

Reproducibility of scratch assays is affected by the initial degree of confluence: Experiments, modelling and model selection

Wang Jin [a], Esha T. Shah [b], Catherine J. Penington [a], Scott W. McCue [a], Lisa K. Chopin [b], Matthew J. Simpson [a,b,*]

[a] School of Mathematical Sciences, Queensland University of Technology (QUT) Brisbane, Queensland, Australia
[b] Ghrelin Research Group, Translational Research Institute, QUT, 37 Kent St, Woolloongabba, Queensland, Australia

HIGHLIGHTS

- Scratch assays with different initial cell densities are performed.
- Rate of re-colonisation is very sensitive to the initial density.
- Calibrating the Fisher Kolmogorov model implies that the cell diffusivity, D, & proliferation rate λ, appear to depend on initial density.
- Calibrating the Porous Fisher model suggests a reduced dependence of D & λ on the initial density.
- In general, our approach suggests that the Porous Fisher model is better suited to our experiments than the Fisher Kolmogorov model.

ARTICLE INFO

Article history:
Received 22 July 2015
Received in revised form
30 September 2015
Accepted 31 October 2015
Available online 29 November 2015

Keywords:
Scratch assay
Reproducibility
Cell diffusivity
Cell proliferation rate

ABSTRACT

Scratch assays are difficult to reproduce. Here we identify a previously overlooked source of variability which could partially explain this difficulty. We analyse a suite of scratch assays in which we vary the initial degree of confluence (initial cell density). Our results indicate that the rate of re-colonisation is very sensitive to the initial density. To quantify the relative roles of cell migration and proliferation, we calibrate the solution of the Fisher–Kolmogorov model to cell density profiles to provide estimates of the cell diffusivity, D, and the cell proliferation rate, λ. This procedure indicates that the estimates of D and λ are very sensitive to the initial density. This dependence suggests that the Fisher–Kolmogorov model does not accurately represent the details of the collective cell spreading process, since this model assumes that D and λ are constants that ought to be independent of the initial density. Since higher initial cell density leads to enhanced spreading, we also calibrate the solution of the Porous–Fisher model to the data as this model assumes that the cell flux is an increasing function of the cell density. Estimates of D and λ associated with the Porous–Fisher model are less sensitive to the initial density, suggesting that the Porous–Fisher model provides a better description of the experiments.

© 2015 Elsevier Ltd. All rights reserved.

1. Introduction

Two-dimensional *in vitro* cell migration assays are routinely used to investigate the ability of cell populations to re-colonise an initially-vacant region. The most common type of *in vitro* cell migration assay is called a scratch assay, which is performed by: (i) growing a cell monolayer; (ii) removing a region of the monolayer by scratching it with a sharp-tipped instrument; and (iii) making observations of the re-colonisation of the initially-vacant, scratched region (Ashby and Zijlstra, 2012; Kramer et al., 2013). Comparing the rate of scratch closure in an experiment where cells are exposed to a chemical stimulus to the rate of closure in a control assay provides insight into the roles of growth factors and putative drug treatments relevant to malignant spreading and tissue repair (Ashby and Zijlstra, 2012; Kramer et al., 2013).

Although scratch assays remain popular, various alternative *in vitro* assays have been proposed. These alternatives, including circular barrier assays (Vo et al., 2015), circular invasion assays (Kam et al., 2008) and IncuCyte ZOOM™ assays (EssenBioScience, 2015), are often claimed to be superior because of issues associated with scratch assay reproducibility (Gough et al., 2011). The purpose of these alternative assays is to reduce some source of

---

* Corresponding author. Tel.: +617 31385241; fax: +617 3138 2310.
E-mail address: matthew.simpson@qut.edu.au (M.J. Simpson).

http://dx.doi.org/10.1016/j.jtbi.2015.10.040
0022-5193/© 2015 Elsevier Ltd. All rights reserved.

variability in the experimental design. For example, standard scratch assays can be performed with various types of instruments (e.g. pipette tip, and razor blade) and with varying degrees of pressure. Each of these variables is thought to have the potential to affect the results in some way. To address these limitations, the IncuCyte ZOOM™ real time live cell imaging assays have been developed (EssenBioScience, 2015). IncuCyte ZOOM™ assays use a mechanical tool, called a WoundMaker™, to create 96 identically-sized scratches in each well of a 96-well tissue culture plate. Each WoundMaker™ scratch has the same dimensions, and is created with the same amount of pressure.

In this work we explore a previously overlooked source of variability that has the potential to impact the interpretation of various types of cell migration assays. While standard experimental procedures for many cell migration assays require that a sufficient amount of time is allowed for the population to become confluent before the experiment is initiated (Ashby and Zijlstra, 2012; Kramer et al., 2013), most experiments do not report any quantitative measurements of the initial degree of confluence (Gujral et al., 2014; Kam et al., 2008; Maini et al. 2004a,b; Sherratt and Murray, 1990). Many experimental protocols simply state that the monolayer is either fully confluent (Kam et al., 2008) or 80% confluent (Bryant et al., 2010) prior to making a scratch. These reports of the *degree of confluence* are typically based on a qualitative judgment rather than quantitative measurements. To investigate the significance of this, we perform a suite of IncuCyte ZOOM™ assays, using PC-3 prostate cancer cells (Kaighn et al., 1979), in which we systematically vary the initial density. A qualitative comparison of the experimental images suggests that the rate of scratch closure is extremely sensitive to the initial density. This dependence on the initial density is important since experimental results are almost always reported without any quantitative measurement of the initial density. This could explain why scratch assays are difficult to reproduce.

We make quantitative measurements of the IncuCyte ZOOM™ assays by extracting cell density profiles and calibrating the solution of the Fisher–Kolmogorov model (Fisher, 1937; Kolmogorov et al., 1937), to that data. This procedure provides an estimate of the cell diffusivity, D, and the cell proliferation rate, λ, for each initial density considered. This procedure is standard; however, typical approaches deal with just one initial density (Cai et al., 2007; Habbal et al., 2014; Maini et al. 2004a,b; Savla et al., 2004; Sengers et al., 2007; Sherratt and Murray, 1990). The appropriately calibrated solutions of the Fisher–Kolmogorov equation match our experimental observations, for each initial density, very well. However, our estimates of D and λ appear to depend upon the initial cell density, and our estimates of D are extremely sensitive. This result has two implications. First, additional mechanisms, unaccounted for in the Fisher–Kolmogorov model, are likely to be acting in the experimental system. To explore this possibility we also examine the suitability of some potential extensions of the Fisher–Kolmogorov model, such as the Porous–Fisher equation (Sherratt and Murray, 1990; Sengers et al., 2007; Simpson et al., 2011; Witelski, 1994,1995). Second, our results suggest that previously reported procedures for estimating D and λ by calibrating the solution of the Fisher–Kolmogorov equation could provide misleading results.

2. Methods

We perform monolayer scratch assays using the IncuCyte ZOOM™ system (Essen BioScience, MI USA). All experiments are performed using the PC-3 prostate cancer cell line (Kaighn et al., 1979) from the American Type Culture Collection (ATCC, Manassas, USA). Cells are propagated in RPMI1640 medium (Life Technologies, Australia) in 10% foetal calf serum (Sigma-Aldrich, Australia), with 100 U/mL penicillin, 100 μg/mL streptomycin (Life Technologies), in plastic flasks (Corning Life Sciences, Asia Pacific) in 5% CO_2 and 95% air in a Panasonic incubator (VWR International) at 37 °C. Cells are regularly screened for *Mycoplasma* (Nested PCR using primers from Sigma-Aldrich).

Cells grown to approximately 80% confluence are removed from the plastic flask using TrypLE™ (Life Technologies) in phosphate buffered saline (pH 7.4), resuspended in medium and seeded at various densities in 96-well ImageLock plates (Essen BioScience). Cells are distributed in the wells as uniformly as possible. We report results for initial cell densities of 10,000, 12,000, 14,000, 16,000, 18,000 and 20,000 cells per well. After seeding, cells are grown overnight to allow for attachment and some growth. We use a WoundMaker™ (Essen BioScience) to create uniform, reproducible scratches in all the wells of a 96-well plate. To ensure that as many cells are removed from the wound region as possible, we modify the manufacturer's protocol by repeating the scratch action 20 times before lifting the WoundMaker™. After creating the scratch, the medium is aspirated and the wells are washed twice with fresh medium to remove cells from the scratched area. Following the washes, 100 μL of fresh medium is added to each well and the plate is placed into the IncuCyte ZOOM™ apparatus. Images of the collective cell spreading are recorded every two hours, for 48 hours. For each different cell density, we perform three identically prepared experimental replicates ($n=3$).

We obtain numerical solutions to various parabolic reaction–diffusion models using a finite difference method (Morton and Mayers, 2005). The spatial domain, $0<x<L_x$, is uniformly discretised with grid spacing δx, and the spatial derivatives are approximated using a central-difference approximation. Some of the models we consider involve a nonlinear diffusion term, which is discretised with an arithmetically averaged inter-node diffusivity. For all models considered, spatial discretisation leads to a system of coupled nonlinear ordinary differential equations that are integrated through time using a backward-Euler approximation with constant time steps of duration δt (Morton and Mayers, 2005). The systems of coupled nonlinear algebraic equations are linearised using Picard (fixed-point) iteration, with absolute convergence tolerance ϵ, and solved using the Thomas algorithm (Morton and Mayers, 2005). For all results we choose δx, δt and ϵ so that our algorithm produces grid-independent results.

3. Results and discussion

3.1. Qualitative assessment of experiments

A subset of the experimental images are presented in Fig. 1 for the experiments initiated with 12,000, 16,000 and 20,000 cells per well. Images in Fig. 1(a), (f) and (k) show that each experiment is initiated with a clean, and sharp scratch. The initial difference in cell density is visually distinct in the regions well behind the position of the scratch. The temporal progression of each experiment is shown in the columns of Fig. 1. In each case we see evidence of combined cell migration and cell proliferation. Cells located near the edge of the scratched region move into the vacant region over time. Cells are also proliferating since we see the cell density behind the location of the scratch increasing with time. Interestingly, if we compare the final images of each experiment, in Fig. 1(e), (j) and (o), a large portion of the initially-vacant wound space in Fig. 1(e) remains uncolonised, whereas the total area imaged in Fig. 1(o) appears to be colonised by $t=48$ h.

Our visual interpretation of these images indicates that the ability of PC-3 cells to re-colonise the wound space is very

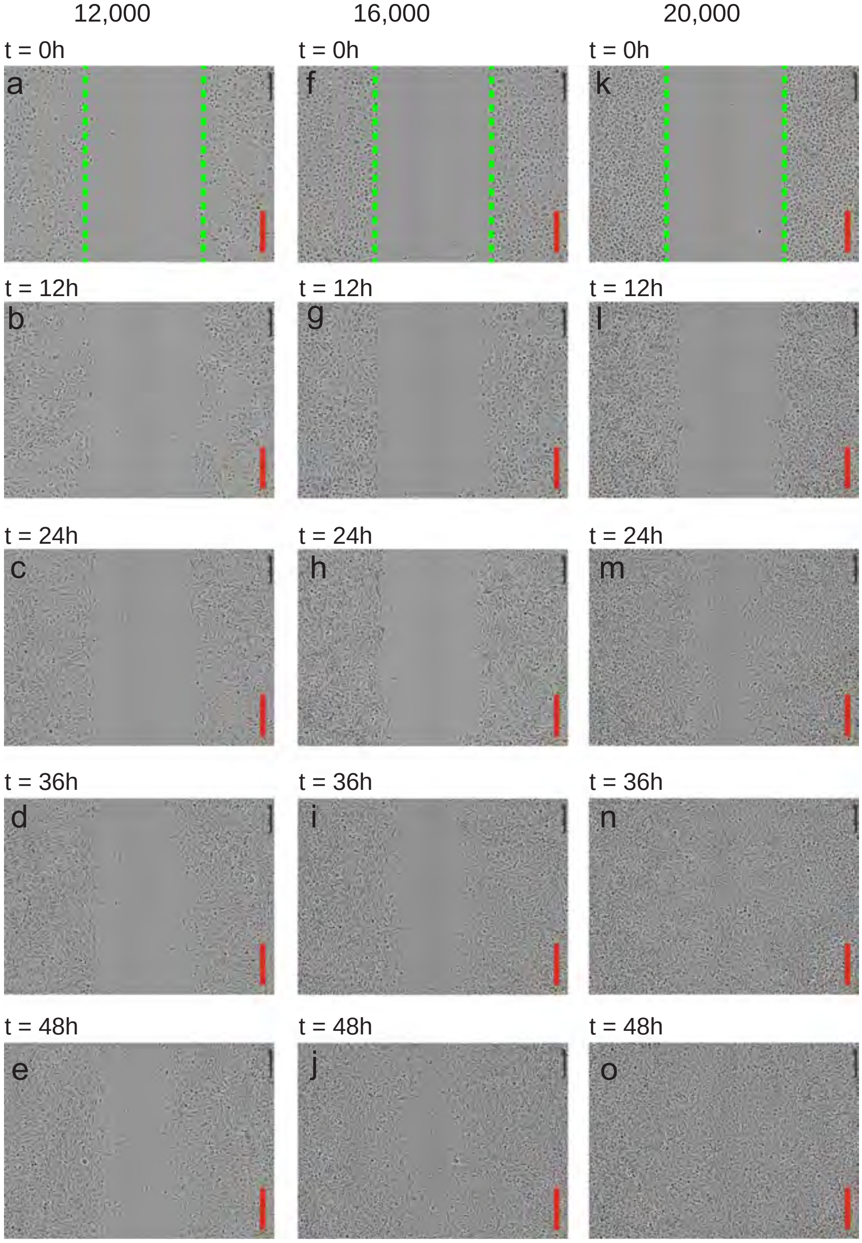

Fig. 1. A summary of IncuCyte ZOOM™ experiments. Images correspond to an experiment initiated with: (a)–(e) 12,000; (f)–(j) 16,000; and (k)–(o) 20,000 cells per well. The time that the image is recorded is indicated on each subfigure and the scale bar corresponds to 300 μm. The images in (a), (f) and (k), at $t = 0$ h, show the approximate location of the position of the leading edge (dashed green).

sensitive to the initial density of cells. This observation is important because many *in vitro* experiments do not report any quantitative measurement of the initial degree of confluence (Gough et al., 2011; Gujral et al., 2014; Kam et al., 2008; Maini et al. 2004a,b), and our results suggest that it would be very difficult to replicate this kind of experiment unless the initial degree of confluence is measured and reported.

Although our visual interpretation of the results in Fig. 1 implies that the rate of closure is very sensitive to the initial density, it is not obvious at this stage whether the differences in the rate of re-colonisation are caused by: (i) differences in the initial cell density alone; (ii) differences in the rate of cell migration; (iii) differences in the rate of cell proliferation; or (iv) differences in both the rates of cell migration and cell proliferation. To address this question, we now interpret our experimental results quantitatively by measuring the temporal evolution of the spatial cell density profiles and using this data to calibrate a suite of mathematical models to the data.

3.2. Quantitative assessment of experiments

We divide each image into 39 equally-spaced columns (Charteris and Khain, 2014; Khain et al., 2011, 2012). Each column is 50 μm wide, as shown in Fig. 2(a). We do not use data from the right most column since the imaging system superimposes a scale bar in that column which partially obscures certain cells. We count the numbers of cells in the remaining columns, $i = 1, 2, 3, \ldots, 38$, and divide the total number of cells per column by the column area to give an estimate of the cell density in each column. We repeat this process for each replicate and calculate the sample mean and sample standard deviation of the cell density in each column for $t = 0, 12, 24, 36$ and 48 h (Supplementary Material Document 2–7). Plots of the mean cell density, with error bars

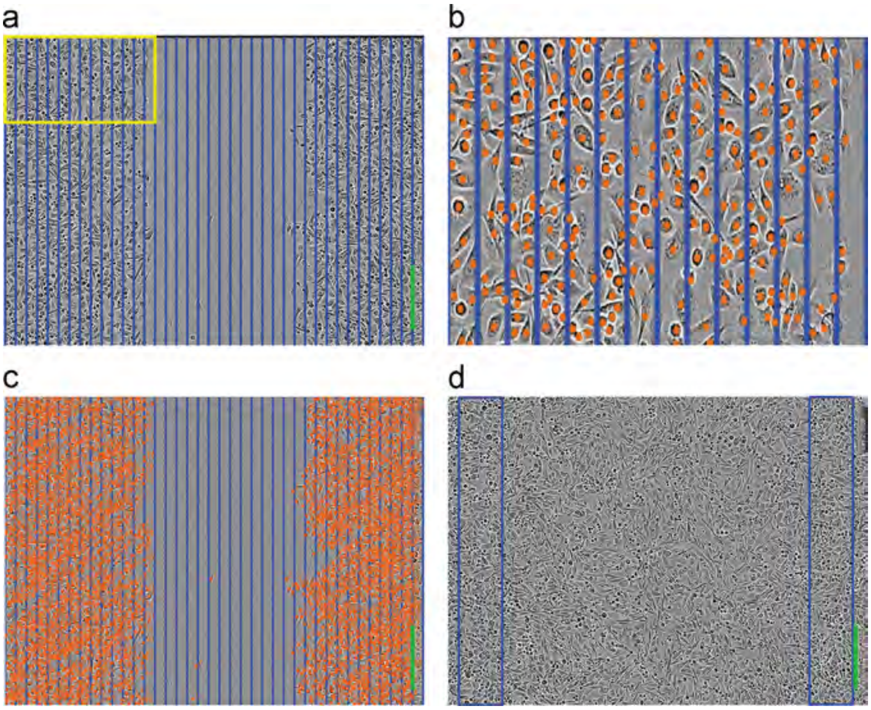

Fig. 2. To quantify the cell density profile, each image is divided into vertical columns of width 50 μm, as shown in (a), from which manual cell counting is used to estimate the cell density at positions $x=25, 75, 125, \ldots, 1925$ μm. To count and record the locations of individual cells we zoom in to focus on certain subregions, such as the subregion shown in (b), which corresponds to the rectangle highlighted in (a). Using the counting features in Adobe Photoshop, we identify individual cells and place a unique marker on each cell (red disk) as shown in (b). After each image is processed in this way we have then identified the location and total number of cells in each image, as shown in (c). The average cell density profile is calculated by averaging results for three identically-prepared experimental replicates. To quantify the carrying capacity density, K, we count the cell density in two regions at $t=48$ h. The locations of the two regions are indicated in (d). These two regions are located well behind the initial position of the leading edge. Estimates of K are obtained using three identically-prepared experimental replicates and the results are averaged to give $K=1.7 \times 10^{-3}$ cells/μm^2. The scale bar in each image corresponds to 300 μm. These particular experimental images correspond to one of the replicates from an experiment initialised with 20,000 cells per well. All parameter estimates reported in this caption are given to two significant figures.(For interpretation of the references to color in this figure legend, the reader is referred to the web version of this article.)

indicating the sample deviation, are given in Fig. 3. In general, we see that the variability between the different experimental replicates for each initial condition is small (Supplementary Material Document 2–7). In contrast, the evolution of the cell density profiles with different initial conditions gives vastly different results. For example, the cell density profiles in Fig. 3(a), shows that the initial location of the scratch, where the local density is approximately zero, is evident after $t=48$ h. In contrast, the profiles in Fig. 3(f) indicate that the population becomes almost uniformly confluent after $t=48$ h. Overall, the general trends in Fig. 3 show that the experiments with a higher initial density leads to a more rapid re-colonisation.

3.3. *Measuring the carrying capacity density K*

The carrying capacity density, $K>0$, is the maximum density for a monolayer of cells. Comparing various cell density profiles in Fig. 3, we see that the experiments initialised with 20,000 cells become more confluent by $t=48$ h than the experiments initialised with smaller numbers of cells. Therefore, to estimate K we focus on the data from experiments initialised with 20,000 cells at $t=48$ h, to ensure that our estimate of K corresponds to a confluent population. We estimate K by calculating the cell density in two subregions, each of width 200 μm, located well-behind the initial position of the front, as indicated in Fig. 2(d). We count the total number of cells in these two subregions and divide by the total area. Repeating this procedure for our three identically-prepared experimental replicates gives: $K=1.71 \times 10^{-3}, 1.74 \times 10^{-3}$ and 1.69×10^{-3} cells/μm^2. Therefore, our estimate is $K=1.7 \times 10^{-3} \pm 2.5 \times 10^{-5}$ cells/μm^2, where the variability is indicated by the sample standard deviation. Since the variability is very small, with the coefficient of variation just 1.5%, our estimate is precise. Our estimate is consistent with previously research. For example, Cai et al. report $K=1.0 \times 10^{-3}$ cells/μm^2 for fibroblasts, whereas Treloar et al. report $K=1.6 \times 10^{-3}$ cells/μm^2 for 3T3 fibroblast cells in a circular barrier assay.

Our estimate of K is consistent with certain features of the cell density profiles in Fig. 3 since our measurements of $C(x,t)$ appear to approach K after a sufficiently large amount of time has elapsed. This is evident in Fig. 3(e), (f) where the population becomes almost uniformly confluent by $t=48$ h and we have $C(x,t) \to K^-$ as t becomes sufficiently large. Since our experimental data contains fluctuations (Supplementary Material Document 2–7). and our estimate of K represents an average, we do occasionally observe estimates of cell density that exceed our estimate of K.

3.4. *Fisher-Kolmogorov model*

The Fisher-Kolmogorov model has been used to describe collective cell spreading in both *in vitro* (Maini et al. 2004a,b; Sherratt and Murray, 1990; Sengers et al., 2007) and *in vivo* (Jackson et al., 2015; Lewis Neal et al., 2013; Rockne et al., 2014) contexts. Calibrating the solution of the Fisher-Kolmogorov model to experimental data can be used to quantify the roles of cell migration and cell proliferation (Maini et al. 2004a,b; Sengers et al., 2007). Given our estimates of the average cell density profiles in Fig. 3 together with our estimate of K, we will calibrate the solution of the Fisher-Kolmogorov model to our data. In this work we apply

$$\frac{\partial C}{\partial t} = \mathcal{D}\frac{\partial^2 C}{\partial x^2} + \lambda C\left[1-\left(\frac{C}{K}\right)\right], \tag{1}$$

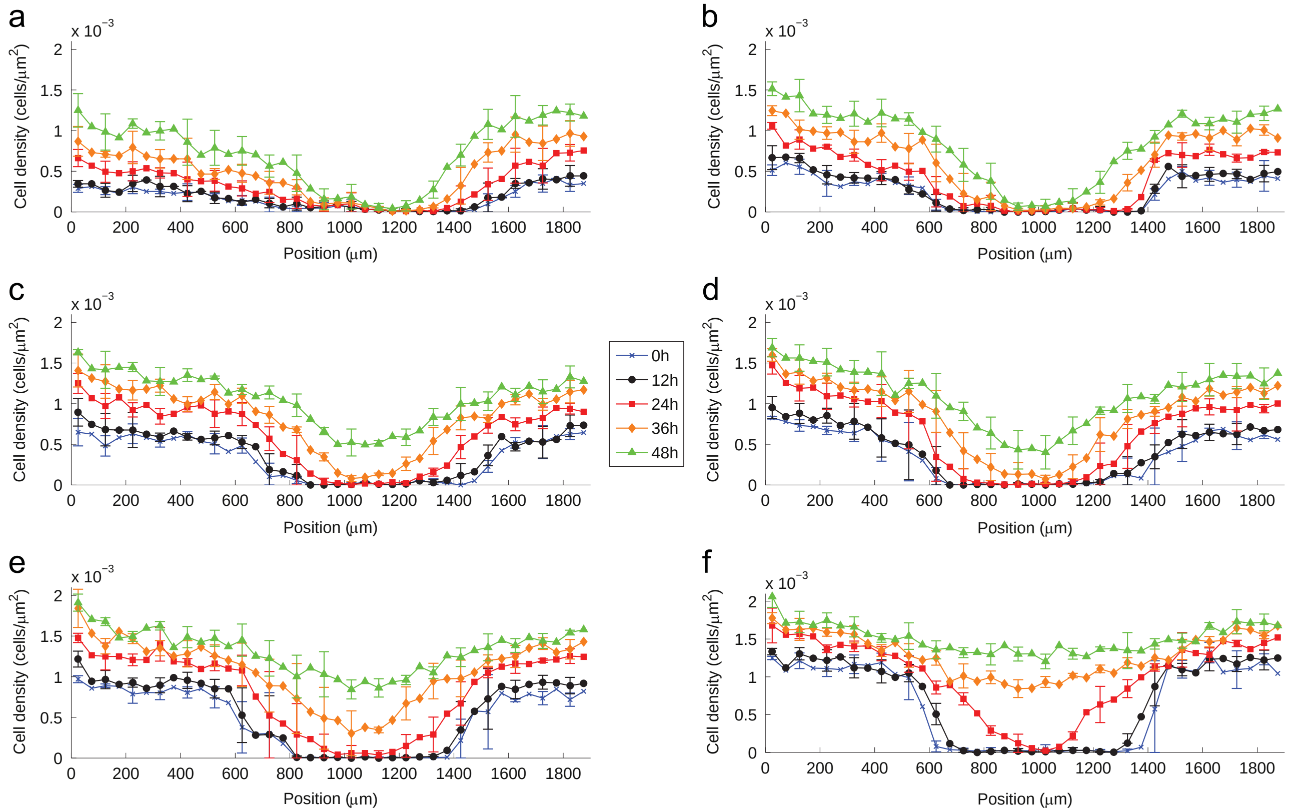

Fig. 3. Cell density profiles. Results in (a)–(f) correspond to experiments initiated with 10,000, 12,000, 14,000, 16,000, 18,000 and 20,000 cells per well, respectively. For each different initial condition, experimental cell density profiles are shown at $t=0$, 12, 24, 36 and 48 h. Each experiment was repeated $n=3$ times. The average density corresponds to the sample mean and the error bars indicate the variability, corresponding to the sample standard deviation.

on $0 \le x \le 1900$ μm, where $\mathcal{D}=D$ is the cell diffusivity and λ is the cell proliferation rate. The cell proliferation rate is related to the cell doubling time, $t_d=\ln(2)/\lambda$. To determine the appropriate boundary conditions for Eq. (1), we recall that the diameter of the 96-well plate is 9000 μm whereas the width of view of the experimental images is just 1950 μm. Therefore, the actual distribution of cells in each well extends far beyond the vertical boundaries of the images in Fig. 1. Since the cells are initially distributed uniformly, and the distribution of cells appears to remain approximately spatially uniform far away from the edges of the scratch for the duration of the experiment, we impose zero net flux boundary conditions at both $x=0$ μm and $x=1900$ μm (Binder and Simpson, 2015). The initial condition for Eq. (1) is specified using the mean cell density data obtained by direct cell counting at $t=0$ h. The data in Fig. 3 at $t=0$ h gives the average cell density at the center of each column in Fig. 2(a), corresponding to $x=25, 75, 125, \ldots, 1875$ μm, for the six different experiments with different initial densities. We specify the continuous initial condition, $C(x,0)$, for the numerical solution of Eq. (1) by linearly interpolating these measurements at $t=0$ h.

While our experiments are genuinely two-dimensional, we always consider a special class of problems where the initial density is, on average, independent of the vertical location in the field of view. Under these conditions it is standard to quantify the cell density profiles by dividing the experimental image into many equally-spaced columns and to report the cell density using a one-dimensional column-averaged cell density and to calibrate the solution of a one-dimensional reaction-diffusion equation to that data (Charteris and Khain, 2014; Khain et al., 2011, 2012). Some of our previous analysis has shown that, in general, there can be an error introduced by approximating a two-dimensional nonlinear reaction-diffusion equation by a vertically-averaged one-dimensional reaction-diffusion equation (Simpson et al., 2009; Simpson, 2009). However, when we consider a special initial condition where the density is independent of vertical location (Fig. 1), the averaging error vanishes (Simpson, 2009).

To estimate D and λ we minimise a least-squares error describing the discrepancy between the solution of Eq. (1) and the average cell density profiles. The least-squares error is given by

$$E(D,\lambda)=\sum_{i=1}^{38}\sum_{j=1}^{4}\left[C^{\text{model}}(x_i,t_j)-C^{\text{data}}(x_i,t_j)\right]^2, \tag{2}$$

where $C^{\text{model}}(x,t)$ is the numerical solution of Eq. (1) and $C^{\text{data}}(x,t)$ is the average cell density data. The index i indicates the position along the x coordinate where the cell density is measured so that $i=1,2,3,\ldots,38$. The index j indicates the time so that $j=1,2,3$ and 4 corresponds to $t=12, 24, 36$ and 48 h. We denote the least-squares estimate of D and λ as $\overline{D}$ and $\overline{\lambda}$, respectively, such that $E(\overline{D},\overline{\lambda})$ is a minimum.

In the literature, cell diffusivities are reported to be in the range of 10–3000 μm²/h (Cai et al., 2007; Vo et al., 2015; Maini et al. 2004a,b; Sengers et al., 2007). Similarly, cell doubling times are typically reported to be within the range of 10–30 h (Johnston et al., 2014). Therefore, we begin our parameter estimation by conservatively limiting our search to within $0 \le D \le 4000$ μm²/h and $0 \le \lambda \le 0.1$/h. Using numerical solutions of Eq. (1), we plot $E(D,\lambda)$ for each set of experimental data in Fig. 4(a)–(f). Each subfigure in Fig. 4(a)–(f) shows $E(D,\lambda)$ constructed by considering a grid of 100 equally-spaced intervals of D, and 50 equally-spaced values of λ. Visual inspection of $E(D,\lambda)$ in Fig. 4(a)–(f) confirms that each error surface appears to contain a well-defined minimum, from which we estimate $\overline{D}$ and $\overline{\lambda}$. After we have obtained our initial estimates using the surfaces in Fig. 4(a)–(f), we refine our estimates by identifying a subregion surrounding the point $(\overline{D},\overline{\lambda})$,

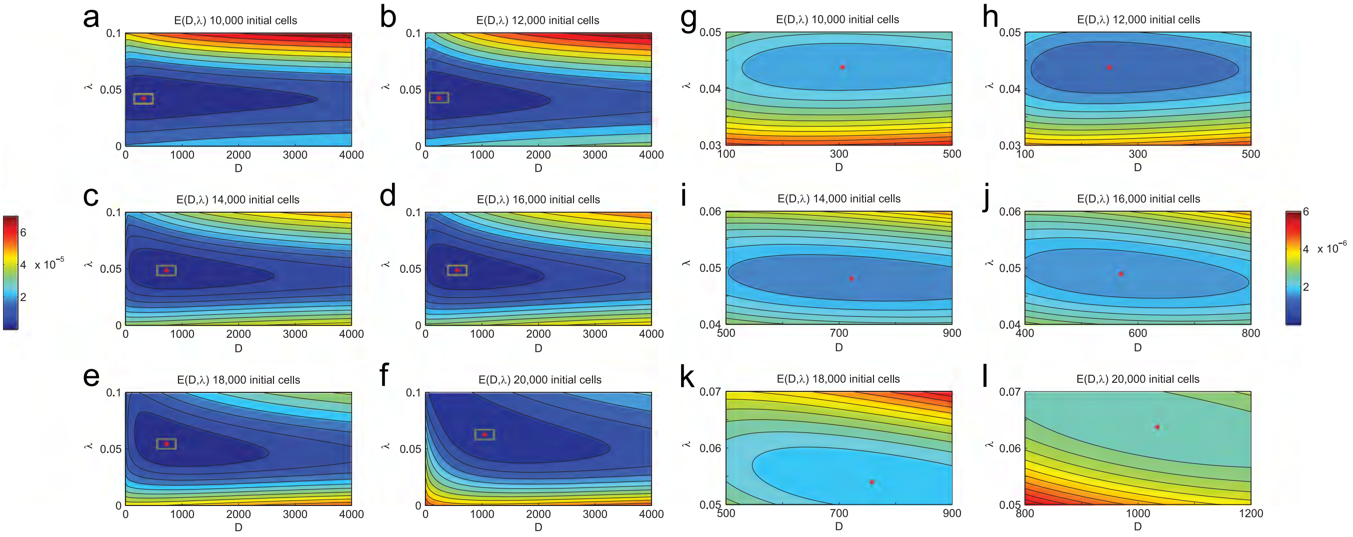

Fig. 4. (a)–(f) Error surface profiles, $E(D,\lambda)$, for the Fisher-Kolmogorov model. The error surface profiles, $E(D,\lambda)$, are constructed using 100 equally-spaced values of D in $0 \le D \le 4000\ \mu\text{m}^2/\text{h}$, and 50 equally-spaced values of λ in $0 \le \lambda \le 0.1/\text{h}$. The value of $E(D,\lambda)$ in (a)–(f) is shown on the left-most colour bar. (g)–(l) Refined estimates of $E(D,\lambda)$ centered about the minima identified in (a)–(f) (white rectangle). The value of $E(D,\lambda)$ in (g)–(l) is shown on the right-most colour bar. The location of $\overline{D}$ and $\overline{\lambda}$ in each case is shown as a red square. Estimates of $(\overline{D},\overline{\lambda})$ correspond to: (a) (320, 0.043), (b) (240, 0.043), (c) (730, 0.049), (d) (570, 0.049), (e) (730, 0.055), (f) (1050, 0.063), (g) (310, 0.044), (h) (250, 0.044), (i) (720, 0.048), (j) (570, 0.049), (k) (760, 0.054), (l) (1030, 0.064). All parameter estimates reported in this caption are given to two significant figures.

Table 1
Estimates of $\overline{D}$ and $\overline{\lambda}$ for the Fisher-Kolmogorov model obtained by calibrating the solution of Eq. (1) to the average cell density profiles for all six different initial conditions. The right-most column gives the doubling time, $t_d = \ln(2)/\overline{\lambda}$. All parameter estimates are given to two significant figures.

Initial number of cells	$\overline{D}$ (μm^2/h)	$\overline{\lambda}$ (/h)	t_d (h)
10,000	310 ± 130	0.044 ± 0.005	15.75
12,000	250 ± 140	0.044 ± 0.002	15.75
14,000	720 ± 60	0.048 ± 0.001	14.44
16,000	570 ± 250	0.049 ± 0.003	14.15
18,000	760 ± 80	0.054 ± 0.003	12.84
20,000	1030 ± 200	0.064 ± 0.001	10.83

shown in Fig. 4(a)–(f) as a white rectangle, and we refine our search within this subregion. Results in Fig. 4(g)–(l) show a refined plot of $E(D,\lambda)$ constructed using a grid of 100 equally-spaced intervals of D and 50 equally-spaced values of λ within the subregions identified in Fig. 4(a)–(f). The refined plots of $E(D,\lambda)$ in Fig. 4(g)–(l) focus on the subregion with $\overline{D}-200 \le D \le \overline{D}+200\ \mu$m^2/h and $\overline{\lambda}-0.01 \le \lambda \le \overline{\lambda}+0.01$/h. Each refined plot of $E(D,\lambda)$ in Fig. 4(g)–(l) also appears to contain a well-defined minimum from which we can identify refined estimates of $(\overline{D},\overline{\lambda})$. Using this approach we found that our refined estimates of $\overline{D}$ and $\overline{\lambda}$ obtained from Figs. 4(g)–(l) are not very different from the original estimates identified in Figs. 4(a)–(f). Therefore, we make no additional refinements, and a summary of our refined estimates is given in Table 1.

To provide an additional check on our estimates of $\overline{D}$ and $\overline{\lambda}$ in Table 1, we also used these estimates, together with our measurements K, as an initial guess for a MATLAB Levenberg Marquardt-based calibration algorithm (Coleman and Li, 1996). We found that applying the MATLAB routine produced parameter estimates that are very similar to those in Table 1, so we do not report any additional results from the MATLAB algorithm here. Instead, we prefer to manually explore the error surface. This allows us to visualise the shape of the error surface, providing us with additional qualitative and quantitative information about the quality of the match between the mathematical model and the experimental data.

Our estimates of D and λ in Table 1 show several interesting trends, the most obvious being that we obtain very different estimates of $\overline{D}$ and $\overline{\lambda}$ for each initial condition. In general, both $\overline{D}$ and $\overline{\lambda}$ increase with the initial density of cells. In particular, we have an approximately 45% variation in $\overline{\lambda}$ and an approximately 310% variation in $\overline{D}$ across the different experiments with different initial conditions. Therefore, our estimates of $\overline{D}$ appear to be more sensitive to variations in the initial density rather than $\overline{\lambda}$. We note that the estimates of $\overline{D}$ and $\overline{\lambda}$ are obtained by calibrating the solution of Eq. (1) to the average cell density profiles shown in Fig. 3. In addition, we also calibrated the solution of Eq. (1) to each of the three individual cell density profiles from each experimental replicate to provide three additional estimates of the cell diffusivity and the cell proliferation rate for each initial density of cells. By calculating the sample standard deviation from these additional estimates we also report, in Table 1, an estimate of the variability in our estimates of $\overline{D}$ and $\overline{\lambda}$ between the three experimental replicates for each different initial cell density. The variability in our estimates of $\overline{D}$ and $\overline{\lambda}$ between each experimental replicate with the same initial density is much smaller than the variability we observe between different experiments with different initial cell density.

To demonstrate the quality of match between the experimental data and the calibrated solution the Fisher-Kolmogorov model, we superimpose, in Fig. 5, the experimental data and the calibrated solution of Eq. (1) for each initial condition. For each of the six different initial conditions we solve Eq. (1) numerically setting $D = \overline{D}$ and $\lambda = \overline{\lambda}$ using the values reported in Table 1. The quality of match between the calibrated Fisher-Kolmogorov equation and the experimental data is excellent.

Our approach of calibrating the Fisher-Kolmogorov model to each data set for the various initial conditions separately reveals several important insights. For example, had we followed a standard approach and studied just one initial condition (e.g. Maini et al. 2004a,b; Sengers et al., 2007), we would have identified estimates of D and λ for which our numerical solution of Eq. (1) would match the experimental data extremely well. However, had another researcher attempted to repeat our experiments and parameter estimation procedure, it is likely that a small change in the initial density could lead to a large change in the estimates of $\overline{D}$ and $\overline{\lambda}$. This is an important limitation since many cell migration

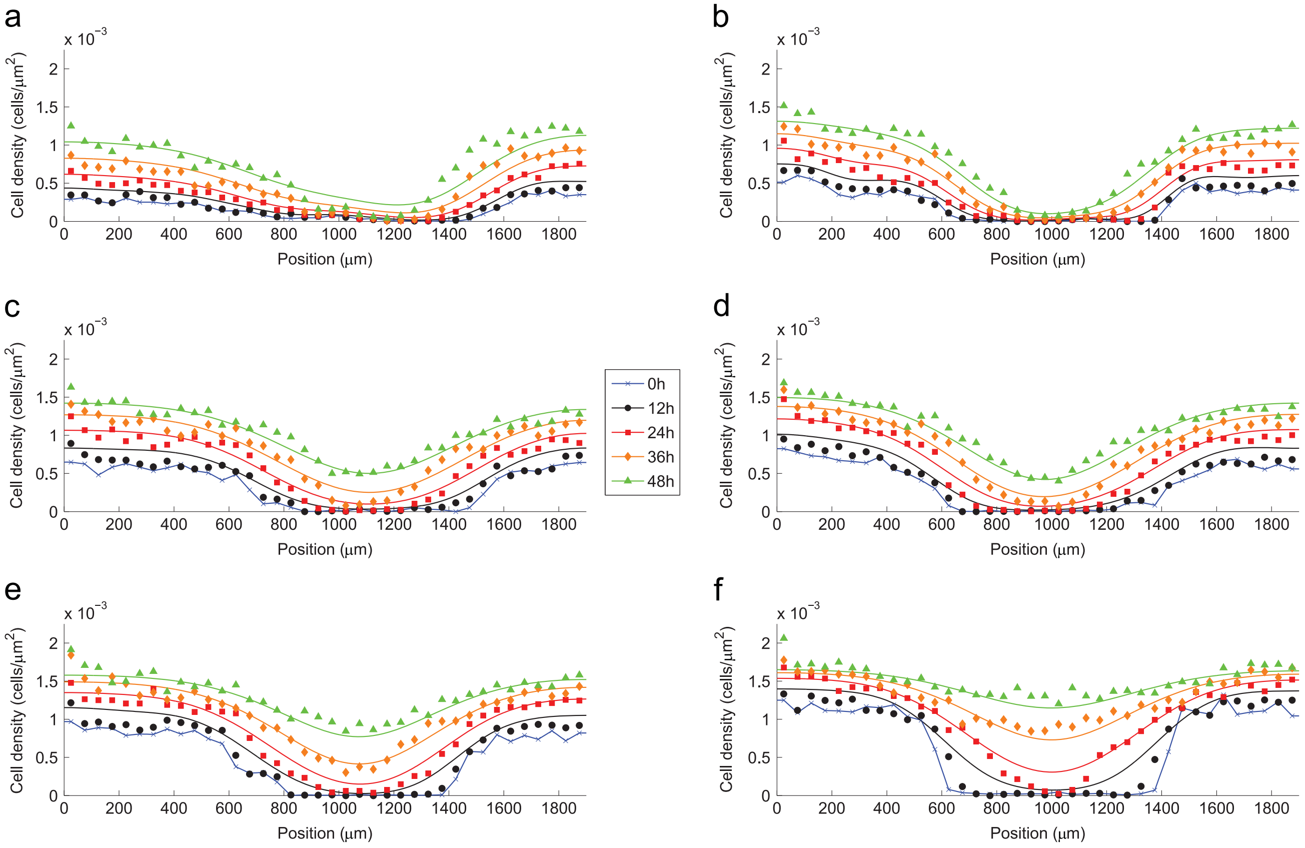

Fig. 5. Calibrated solutions of Eq. (1) to the averaged cell density profiles. Results in (a)–(f) show the average cell density for experiments initiated with 10,000, 12,000, 14,000, 16,000, 18,000 and 20,000 cells per well. In each experiment profiles at $t = 0$, 12, 24, 36 and 48 h are shown. The solid lines correspond to the solution of Eq. (1) with the least squares estimates of $\overline{D}$ and $\overline{\lambda}$ from Table 1. All results correspond to $K = 1.7 \times 10^{-3}$ cells/μm^2 and the numerical solution of Eq. (1) is obtained with $\delta x = 0.25$ μm, $\delta t = 0.2$ h and $\epsilon = 10^{-5}$.

assays neglect to measure the initial density (e.g. Gujral et al., 2014; Maini et al. 2004a,b; Sherratt and Murray, 1990). Therefore, given the extreme sensitivity of the experimental outcomes to the initial density, it is essential that the initial degree of confluence ought to be measured and reported if the experiment is to be reproductive.

Our finding, that $\overline{D}$ and $\overline{\lambda}$ appear to depend on the initial density, implies that the Fisher-Kolmogorov model does not apply to our experimental system. Since the Fisher-Kolmogorov model has constant coefficients, an implicit assumption in the application of this model is that D and λ are independent of the cell density. However, we find that $\overline{D}$ and $\overline{\lambda}$ are very sensitive to the initial density. This motivates us to consider what kind of additional mechanisms might be relevant. One particular criticism of the Fisher-Kolmogorov model is that the linear diffusion term neglects to account for any cell-to-cell adhesion effects (Anguige and Schmeiser, 2009; Deroulers et al., 2009, Khain et al., 2011, 2012; Nardini et al., 2015). It is of interest to note that our experimental results imply that higher initial density leads to enhanced cell spreading (Fig. 1). This is inconsistent with the idea that cell-to-cell adhesion plays an important role in our experiments, since larger initial cell densities would lead to more frequent cell-to-cell collisions and adhesion would lead to a reduced collective spreading of the population. To capture potential adhesive effects, many continuum models take the form of a nonlinear diffusion mechanism where the cell diffusivity, $\mathcal{D}$, is a decreasing function of C (Anguige and Schmeiser, 2009; Deroulers et al., 2009; Khain et al., 2011**; ?**Nardini et al., 2015). In contrast, our results imply that larger initial cell density is associated with increased cell spreading. This motivates us to consider a model in which $\mathcal{D}$ is an increasing function of C.

3.5. Porous-Fisher model

Although many studies have examined various theoretical aspects of extensions of the traditional constant coefficient Fisher-Kolmogorov model (e.g. Curtis and Bortz, 2012; Harris, 2004; Hammond and Bortz, 2011; Witelski 1994,1995), less attention has been devoted to determining whether collective cell spreading is best modelled using the constant coefficient Fisher-Kolmogorov model or a variable coefficient generalisation of the Fisher-Kolmogorov model. We will now briefly survey the most relevant studies that have begun to explore this question. Maini et al. (2004a,b) model the motion of the position of the cell front in an *in vitro* scratch assay using the Fisher-Kolmogorov equation. Although they find that the Fisher-Kolmogorov model is consistent with their experimental observations, they conclude by suggesting that their analysis could be improved by considering the Porous-Fisher model in which the cell flux is governed by a nonlinear diffusion term $\mathcal{D} = D(C/K)$, so that the diffusivity increases with C. Sherratt and Murray model the closure of a radial wound using both the Fisher-Kolmogorov equation and the Porous-Fisher model. Sherratt and Murray find that both reaction-diffusion models can be used to replicate their experimental observations. Similarly, Sengers et al. (2007) collect data from two different cell types in a series of *in vitro* cell spreading experiments and calibrate the solutions of the Fisher-Kolmogorov and Porous-Fisher equations to their data. Sengers et al. find that the Fisher-Kolmogorov model fits the experimental data for one particular cell line very

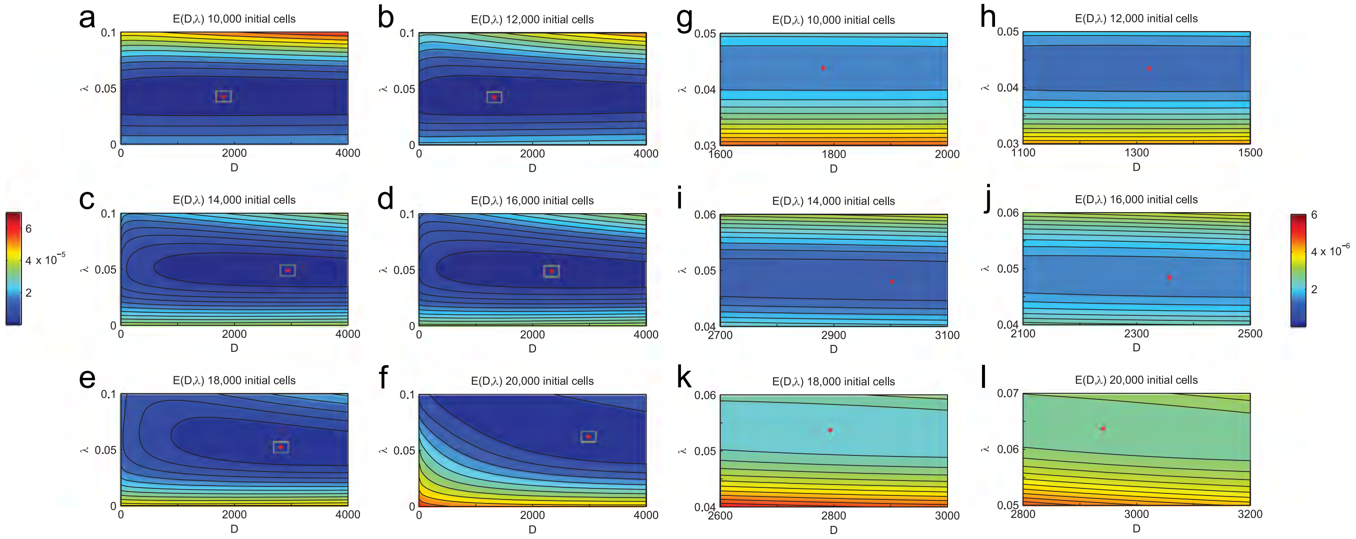

Fig. 6. (a)–(f) Error surface profiles, $E(D,\lambda)$, for the Porous-Fisher model. The error surface profiles, $E(D,\lambda)$, are constructed using 100 equally-spaced values of D in $0 \le D \le 4000\ \mu\text{m}^2/\text{h}$ and 50 equally-spaced values of λ in $0 \le \lambda \le 0.1/\text{h}$. The value of $E(D,\lambda)$ in (a)–(f) is shown on the left-most colour bar. (g)–(l) Refined estimates of $E(D,\lambda)$ centered about the minimum identified in (a)–(f) (white rectangle). The value of $E(D,\lambda)$ in (g)–(l) is shown on the right-most colour bar. The location of $\overline{D}$ and $\overline{\lambda}$ in each case is shown as a red square. Estimates of $(\overline{D},\overline{\lambda})$ correspond to: (a) (1800, 0.043), (b) (1300, 0.043), (c) (2900, 0.049), (d) (2300, 0.049), (e) (2800, 0.053), (f) (3000, 0.063), (g) (1800, 0.044), (h) (1300, 0.043), (i) (3000, 0.048), (j) (2400, 0.049), (k) (2800, 0.054), and (l) (2900, 0.064). All parameter estimates reported in this caption are given to two significant figures.(For interpretation of the references to color in this figure legend, the reader is referred to the web version of this article.)

well, whereas the Porous-Fisher model fits the experimental data for the other cell line very well. This suggests that some cell lines might be best described by the Fisher-Kolmogorov model while others might be best described by the Porous-Fisher model. While these four previous studies are unique in that they directly compare the relative performance of the Fisher-Kolmogorov and Porous-Fisher models, we note that they did not consider the impact of varying the initial density of cells in their experimental system (Maini et al. 2004a,b; Sengers et al., 2007; Sherratt and Murray, 1990).

We now calibrate the solution of the Porous-Fisher model to our data. For our work we consider

$$\frac{\partial C}{\partial t} = D\frac{\partial}{\partial x}\left[\left(\frac{C}{K}\right)\frac{\partial C}{\partial x}\right] + \lambda C\left[1-\left(\frac{C}{K}\right)\right], \qquad (3)$$

on $0 \le x \le 1900\ \mu\text{m}$. We impose the same initial and boundary conditions used in Section 3.4. The only difference between Eqs. (1) and (3) is the nonlinear diffusion mechanism in Eq. (3), where $\mathcal{D} = D(C/K)$. In particular, both models contain the same two unknown parameters: D and λ.

To estimate D and λ in Eq. (3) we followed a similar approach that we use when working with Eq. (1) by plotting $E(D,\lambda)$, given by Eq. (2), and restricting the range of D and λ to be the same as before. The error surfaces in Figs. 4 and 6 appear to be different. For example, the error surface in Fig. 6(a) has a less well defined minimum than the surface in Fig. 4(a). The error surface in Fig. 6 (a) contains a valley-shaped region, parallel to the D-axis, whereas the surface in Fig. 4(a) does not. Regardless of this difference, we follow the same procedure used previously to identify $\overline{D}$ and $\overline{\lambda}$ in Fig. 6(a)–(f). We also refine our estimates by identifying a subregion about the point $(\overline{D},\overline{\lambda})$ in Fig. 6(a)–(f) and plotting $E(D,\lambda)$ centered about this point in Fig. 6(g)–(l). Estimates of $\overline{D}$ and $\overline{\lambda}$ from the refined subregion in Fig. 6(g)–(l) are given in Table 2.

Our estimates of $\overline{\lambda}$ for the Porous-Fisher model are very similar to our estimates for the Fisher-Kolmogorov model, and we observe a variation in $\overline{\lambda}$ of approximately 49% between the different initial conditions. We also observe a variation in our estimates of $\overline{D}$ for the Porous-Fisher model of approximately 130%, which is much smaller than the variation in $\overline{D}$ for the Fisher-Kolmogorov model. To demonstrate the quality of match between the experimental data and the solution the Porous-Fisher model we superimpose, in Fig. 7, the experimental data and the solution of Eq. (3) for each initial condition, and in each case we solve Eq. (3) numerically with $D = \overline{D}$ and $\lambda = \overline{\lambda}$ reported in Table 2. The quality of match between the calibrated Porous-Fisher equation and the experimental data is excellent.

Table 2
Estimates of $\overline{D}$ and $\overline{\lambda}$ for the Porous-Fisher model obtained by calibrating the solution of Eq. (3) to the average cell density profiles for all six different initial conditions. The right-most column gives the doubling time, $t_d = \ln(2)/\overline{\lambda}$. All parameter estimates are given to two significant figures.

Initial number of cells	$\overline{D}$ (μm^2/h)	$\overline{\lambda}$ (/h)	t_d (h)
10,000	1800 ± 1050	0.044 ± 0.005	15.75
12,000	1300 ± 930	0.043 ± 0.002	16.12
14,000	3000 ± 190	0.048 ± 0.001	14.44
16,000	2400 ± 990	0.049 ± 0.003	14.15
18,000	2800 ± 100	0.054 ± 0.004	12.84
20,000	2900 ± 620	0.064 ± 0.002	10.83

The question of whether our experimental data is best described by the Fisher-Kolmogorov or the Porous-Fisher model is a delicate one. Since our estimates of $\overline{D}$ and $\overline{\lambda}$ for the Porous-Fisher model are less sensitive to the initial density than for the Fisher-Kolmogorov model, it appears that the Porous-Fisher model provides a better description of our experimental data. Although the Porous-Fisher model is preferable in this regard, our parameter estimation procedure still implies that $\overline{D}$ and $\overline{\lambda}$ appear to depend on the initial density of cells for the Porous-Fisher model, suggesting that further model refinements could be warranted. Some previous studies suggest a further generalisation of the Porous-Fisher model where the nonlinear diffusivity function is generalised to $\mathcal{D} = D(C/K)^m$ (Harris, 2004; Sherratt and Murray, 1990). This means that setting $m = 0$ in the generalised Porous-Fisher model corresponds to the Fisher-Kolmogorov model. We also calibrate solutions of the Porous-Fisher model to our data with $m = 1/2$, 2, 3 and 4. The calibrated model provides a poor match to the data with $m = 2$, 3 and 4, whereas we observe a good match with $m = 1/2$ and $m = 1$. The variation in $\overline{D}$ and $\overline{\lambda}$ is smaller for $m = 1$ than for $m = 1/2$, and therefore we conclude that the standard Porous-Fisher model with

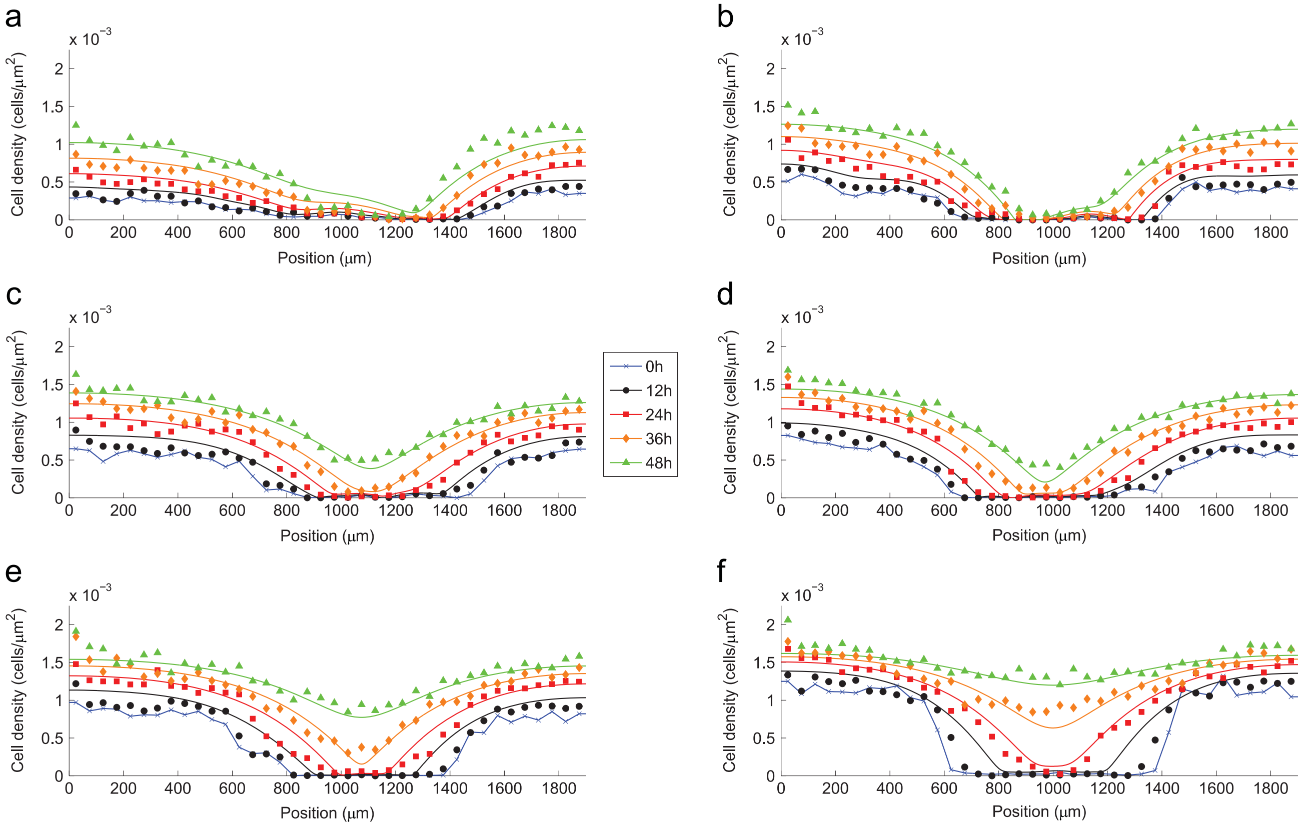

Fig. 7. Calibrated solutions of Eq. (3) to the averaged cell density profiles. Results in (a)–(f) show the average cell density (circles) for experiments initiated with 10,000, 12,000, 14,000, 16,000, 18,000 and 20,000 cells per well. In each experiment profiles at $t=0$, 12, 24, 36 and 48 h are shown. The solid lines correspond to the solution of Eq. (3) with the least squares estimates of D and λ from Table 2. All results correspond to $K=1.7\times10^{-3}$ cells/μm² and the numerical solution of Eq. (3) is obtained with $\delta x=0.25$ μm, $\delta t=0.2$ h and $\epsilon=10^{-5}$.

$m=1$ outperforms the generalised Porous-Fisher model with the other values of m that we consider (Supplementary Material Document 1) . We also consider calibrating a model of chemokinesis to our data (Supplementary Material Document 1) and demonstrate that this kind of detailed, coupled model, also has the potential to describe our experimental data.

4. Conclusions

In this work we explore a previously overlooked source of variability which affects the reproducibility of scratch assays. In a standard experiment, the initial degree of confluence is neither measured or varied (Ashby and Zijlstra, 2012; Kramer et al., 2013). To explore the significance of this, we perform a suite of cell migration assays in which we deliberately vary the initial cell density. Our results show that the rate of re-colonisation is extremely sensitive to the initial density. Therefore, if a scratch assay is to be reproducible, the initial density must be measured and reported.

To quantify the rate of cell migration and proliferation we use a cell counting procedure to estimate the average cell density profiles and the carrying capacity density, K. Estimates of $\overline{D}$ and $\overline{\lambda}$ are obtained by calibrating the Fisher-Kolmogorov model to the data for each initial condition. The calibrated solutions of the Fisher-Kolmogorov model match the experimental cell density profiles, for each initial condition, very well. However, comparing estimates of $\overline{D}$ and $\overline{\lambda}$ for different initial conditions shows that different initial conditions lead to very different estimates of $\overline{D}$ and $\overline{\lambda}$. In particular, $\overline{\lambda}$ varies by approximately 45% whereas $\overline{D}$ varies by approximately 310% across our six different initial conditions. This result is novel since previous studies have considered just one initial condition, and our results show that this standard approach can give very misleading results.

Since our data implies that larger initial cell densities lead to enhanced migration, we calibrate the Porous-Fisher model, with $\mathcal{D}(C)=D(C/K)$, to our data. This exercise shows that the Porous-Fisher model matches the evolution of each of our experiments with estimates of $\overline{D}$ and $\overline{\lambda}$ that are less variable between experiments with different initial conditions than the standard Fisher-Kolmogorov model, suggesting that the Porous-Fisher model provides an improved match to our experimental data. To explore further potential refinements, we also calibrated other reaction-diffusion models to the data, but we found that these extensions offered no advantage over the Porous-Fisher model (Supplementary Material Document 1). Another feature of our analysis is that the error surfaces are more sensitive to variations in λ than D. This could be associated with the way that we have imaged and analysed the experiments. Most of the cells in the field of view are associated with the dense unscratched regions where the dynamics of the experiments are largely associated with proliferation rather than migration. This means that we characterise D using data from the scratched region where the density is, by definition, low, and hence more variable. This could explain why the error surfaces tend to be more dependent on λ than D.

All of the extensions of the Fisher-Kolmogorov model that we consider deal with introducing more detail into the flux term of the reaction-diffusion model. We deliberately choose to focus on the flux term because our estimates of $\overline{D}$ are far more sensitive to variations in the initial condition than $\overline{\lambda}$ in the proliferation term. In principle, it is possible to examine other extensions where the proliferation term, $\lambda C(1-C/K)$, is generalised to $\lambda C^{\alpha}(1-[C/K]^{\beta})^{\gamma}$, where α, β and γ are real positive constants (Tsoularis and Wallace, 2002). We do not pursue this idea here because the variation in $\overline{\lambda}$ for the six different initial conditions is much smaller compared to the variation in $\overline{D}$.

In summary, our study reveals insights that have both experimental and mathematical significance. From an experimental point of view, our results give a partial explanation about why scratch assays are difficult to reproduce. We recommend that measurements of the initial cell density must be reported when describing the outcomes of a scratch assay. From a mathematical point of view we show that a standard approach of calibrating the solution of the Fisher-Kolmogorov model to a scratch assay with a single initial condition can produce misleading estimates of $\overline{D}$ and $\overline{\lambda}$. Since our estimates of $\overline{D}$ and $\overline{\lambda}$ appear to depend on the initial cell density, we suggest that a refined version of this constant coefficient model is warranted and we show that calibrating the Porous-Fisher model to our data leads to an improved outcome in this regard.

Acknowledgements

This work is supported by the Australian Research Council (DP140100249, and FT130100148), the National Health and Research Council (Australia), the Movember Foundation, and the Prostate Cancer Foundation of Australia through a Movember Revolutionary Team Award. We appreciate the thoughtful comments from three anonymous referees.

Appendix A. Supplementary data

Supplementary data associated with this article can be found in the online version at http://dx.doi.org/10.1016/j.jtbi.2015.10.040.

References

Anguige, K., Schmeiser, C., 2009. A one-dimensional model of cell diffusion and aggregation, incorporating volume filling and cell-to-cell adhesion. J. Math. Biol. 58, 395–427.

Ashby, W.J., Zijlstra, A., 2012. Established and novel methods of interrogating two-dimensional cell migration. Integr. Biol. 4, 1338–1350.

Binder, B.J., Simpson, M.J., 2015. Spectral analysis of pair-correlation bandwidth: application to cell biology images. R. Soc. Open Sci. 2, 140494.

Bryant, C.S., Kumar, S., Chamala, S., Shah, J., Pal, J., Haider, M., Seward, S., Qazi, A.M., Morris, R., Semaan, A., Shammas, M.A., Steffes, C., Potti, R.B., Prasad, M., Weaver, D.W., Batchu, R.B., 2010. Sulforaphane induces cell cycle arrest by protecting RB-E2F-1 complex in epithelial ovarian cancer cells. Mol. Cancer 9, 47.

Cai, A.Q., Landman, K.A., Hughes, B.D., 2007. Multi-scale modeling of a wound-healing cell migration assay. J. Theor. Biol. 245, 576–594.

Charteris, N., Khain, E., 2014. Modeling chemotaxis of adhesive cells: stochastic lattice approach and continuum description. New J. Phys. 16, 025002.

Coleman, T.F., Li, Y., 1996. An interior, trust region approach for nonlinear minimization subject to bounds. SIAM J. Optimiz. 6, 418–445.

Curtis, C.W., Bortz, D.M., 2012. Propagation of fronts in the Fisher-Kolmogorov equation with spatially varying diffusion. Phys. Rev. E 86, 066108.

Deroulers, C., Aubert, M., Badoual, M., Grammaticos, B., 2009. Modeling tumor cell migration: from microscopic to macroscopic models. Phys. Rev. E 79, 031917.

EssenBioScience: IncuCyte ZOOM. ⟨http://www.essenbioscience.com/essen-products/incucyte/⟩ (Accessed: September 2015).

Fisher, R.A., 1937. The wave of advance of advantageous genes. Ann. Eugen. 7, 353–369.

Gough, W., Hulkower, K., Lynch, R., Mcglynn, P., Uhlik, M., YanL, Lee J., 2011. A quantitative, facile, and high-throughput image-based cell migration methods is a robust alternative to the scratch assay. J. Biomol. Screen. 16, 155–163.

Gujral, T.S., Chan, M., Peshkin, L., Sorger, P.K., Kirschner, M.W., MacBeath, G., 2014. A noncanonical frizzled2 pathway regulates epithelial-mesenchymal transition and metastasis. Cell 159, 844–856.

Habbal, A., Barelli, H., Malandin, G., 2014. Assessing the ability of the 2D Fisher-KPP equation to model cell-sheet wound closure. Math. Biosci. 252, 45–59.

Hammond, J.F., Bortz, D.M., 2011. Analytical solutions to Fisher's equation with time-variable coefficients. Appl. Math. Comput. 218, 2497–2508.

Harris, S., 2004. Fisher equation with density-dependent diffusion: special solutions. J. Phys. A. 37, 6267–6268.

Jackson, P.R., Juliano, J., Hawkins-Daarud, A., Rockne, R., Swanson, K.R., 2015. Patient-specific mathematical neuro-oncology: using a simple proliferation and invasion tumor model to inform clinical practice. Bull. Math. Biol. 77, 846–856.

Johnston, S.T., Simpson, M.J., McElwain, D.L.S., 2014. How much information can be obtained from tracking the position of the leading edge in a scratch assay? J. R. Soc. Interface 11, 20140325.

Kaighn, M.E., Narayan, K.S., Ohnuki, Y., Lechner, J.F., Jones, L.W., 1979. Establishment and characterization of a human prostatic carcinoma cell line (PC-3). Invest. Urol. 17, 16–23.

Kam, Y., Guess, C., Estrada, L., Weidow, B., Quaranta, V., 2008. A novel circular invasion assay mimics *in vivo* invasive behavior of cancer cell lines and distinguishes single-cell motility in vitro. BMC Cancer 8, 198–210.

Kolmogorov, A., Petrovsky, I., Piscounov, N., 1937. Étude de l'équation de la diffusion avec croissance de la quantité de matière et son application á un probléme biologique. Mosc. Univ. Bull. Math. 1, 1–25.

Khain, E., Katakowski, M., Hopkins, S., Szalad, A., Zheng, X., Jiang, F., Chopp, M., 2011. Collective behavior of brain tumor cells: the role of hypoxia. Phys. Rev. E 83, 031920.

Khain, E., Katakowski, M., Charteris, N., Jiang, F., Chopp, M., 2012. Migration of adhesive glioma cells: front propagation and fingering. Phys. Rev. E 86, 011904.

Kramer, N., Walzl, A., Unger, C., Rosner, M., Krupitza, G., Hengstschlager, M., Dolznig, H., 2013. *In vitro* cell migration and invasion assays. Mut. Res. -Rev. Mutat. 752, 10–24.

Lewis Neal, M., Trister, A.D., Ahn, S., Baldock, A., Bridge, C.A., Guyman, L., Lange, J., Sodt, R., Cloke, T., Lai, A., Coughesy, T.F., Mrugala, M.M., Rockhill, J.K., Rockne, R. C., Swanson, K.R., 2013. Response classification based on a minimal model of glioblastoma growth is prognostic for clinical outcomes and distinguishes progression from pseudoprogression. Cancer Res. 73, 2976–2986.

Maini, P.K., McElwain, D.L.S., Leavesley, D.I., 2004a. Traveling wave model to interpret a wound-healing cell migration assay for human peritoneal mesothelial cells. Tissue Eng. 10, 475–482.

Maini, P.K., McElwain, D.L.S., Leavesley, D.I., 2004b. Travelling waves in a wound healing assay. Appl. Math. Lett. 17, 575–580.

Morton, K.W., Mayers, D.F., 2005. Numerical Solution of Partial Differential Equations. Cambridge University Press, Cambridge.

Nardini, J.T., Chapnick, D.A., Liu, X., Bortz, D.M., 2015. The effects of MAPK activity on cell-cell adhesion during wound healing. arXiv:1506.07081.

Rockne, R.C., Trister, A.D., Jacobs, J., Hawkins-Daarud, A.J., Neal, M.L., Hendrickson, K., Mrugala, M.M., Rockhill, J.K., Kinahan, P., Krohn, K.A., Swanson, K.R., 2014. A patient-specific computational model of hypoxia-modulated radiation resistance in glioblastoma using ^{18}F-FMISO-PET. J. R. Soc. Interface 12, 20141174.

Savla, U., Olson, L.E., Waters, C.M., 2004. Mathematical modeling of airway epithelial wound closure during cyclic mechanical strain. J. Appl. Phys. 96, 566–574.

Sengers, B.G., Please, C.P., Oreffo, R.O.C., 2007. Experimental characterization and computational modelling of two-dimensional cell spreading for skeletal regeneration. J. R. Soc. Interface 4, 1107–1117.

Sherratt, J.A., Murray, J.D., 1990. Models of epidermal wound healing. Proc. R. Soc. B 241, 29–36.

Simpson, M.J., Landman, K.A., Hughes, B.D., 2009. Multi-species simple exclusion processes. Physica A 388, 399–406.

Simpson, M.J., 2009. Depth-averaging errors in reactive transport modeling. Water Resour. Res. 45, W02505.

Simpson, M.J., Baker, R.E., McCue, S.W., 2011. Models of collective cell spreading with variable cell aspect ratio: a motivation for degenerate diffusion models. Phys. Rev. E 83, 021901.

Tsoularis, A., Wallace, J., 2002. Analysis of logistic growth models. Math. Biosci. 179, 21–55.

Vo, B.N., Drovandi, C.C., Pettitt, A.N., Simpson, M.J., 2015. Quantifying uncertainty in parameter estimates for stochastic models of collective cell spreading using approximate Bayesian computation. Math. Biosci. 263, 133–142.

Witelski, T.P., 1994. An asymptotic solution for traveling waves of a nonlinear-diffusion Fisher's equation. J. Math. Biol. 33, 1–16.

Witelski, T.P., 1995. Merging traveling waves for the Porous-Fisher's equation. Appl. Math. Lett. 4, 57–62.